

# Robust Estimation of Field Inhomogeneity Map Following Magnitude-Based Water-Fat Separation with Resolved Ambiguity

Alexandre Triay Bagur<sup>1,2\*</sup>, Darryl McClymont<sup>2</sup>, Chloe Hutton<sup>2</sup>, Andrea Borghetto<sup>2</sup>, Michael L Gyngell<sup>2</sup>, Paul Aljabar<sup>2</sup>, Matthew D Robson<sup>2</sup>, Michael Brady<sup>2</sup>, Daniel P Bulte<sup>1</sup>

<sup>1</sup>Department of Engineering Science, University of Oxford, Oxford, UK

<sup>2</sup>Perspectum Ltd, Oxford, UK

\*[alexandre.triaybagur@eng.ox.ac.uk](mailto:alexandre.triaybagur@eng.ox.ac.uk)

## Abstract

**PURPOSE:** To extend magnitude-based PDFF (Proton Density Fat Fraction) and R2\* mapping with resolved water-fat ambiguity to calculate a B<sub>0</sub> field inhomogeneity map (field map) when phase images are accessible and reliable.

**THEORY:** The estimation is formulated in matrix form, resolving the field map in a least-squares sense. PDFF and R2\* from magnitude fitting may be updated using the estimated field maps.

**METHODS:** The limits of quantification of our voxel-independent implementation were assessed. Bland-Altman was used to compare PDFF and field maps from the proposed method against a reference complex-based method on 152 UK Biobank subjects (1.5 T Siemens). 1 separate acquisition (3 T Siemens) presenting high field inhomogeneities was used for assessment of robustness.

**RESULTS:** Field mapping was accurate beyond the complex-based limit range and up to  $\pm\Delta f$ . High agreement was obtained between the proposed method and the reference method in UK Biobank (PDFF bias = -0.02 %, LoA (limits of agreement) [-0.1,0.1] %; Field map bias = -0.05 Hz, LoA = [-0.2,0.3] Hz). Robust field mapping was observed at 3 T, for inhomogeneities over 300 Hz including rapid variation across edges. Fat-water swaps were observed in complex-based results.

**CONCLUSION:** Field mapping following magnitude-based water-fat separation showed potential in high field inhomogeneities, where complex-based methods struggled.

## Keywords

Proton density fat fraction, MRI-PDFF, fat-water swap, quantitative susceptibility mapping

## Acknowledgement

The authors acknowledge the use of the Fat-Water Toolbox for some of the results shown in this article. The authors acknowledge the use of code from Dr Mark Bydder for the PRESCO algorithm implementation available online for some of the results shown in this article. The authors thank the Engineering and Physical Sciences Research Council (EPSRC) for funding via a doctoral studentship (project reference 2280970). This research has been conducted using the UK Biobank Resource under application 9914. This publication is our view, and the Executive Agency for Small and Medium-sized Enterprises is not responsible for any use of the information herein.

## Data Availability Statement

Publicly available 1.5 tesla data from the UK Biobank study was analyzed in this work. The UK Biobank datasets are available to researchers through an open application via <https://www.ukbiobank.ac.uk/register-apply/>. The additional 3 tesla dataset that supports the findings of this study was de-identified and is openly available to researchers on Zenodo under <https://doi.org/10.5281/zenodo.6652300>.

## Conflict of Interest Statement

ATB, DMC, CH, AB, MLG, MDR, MB are employees of Perspectum and/or hold shares in the company. DPB declares no potential conflict of interest.

## Introduction

Chemical-shift encoded (CSE) MRI water-fat separation methods have emerged as non-invasive tools for proton density fat fraction (MRI-PDFF or PDFF) and  $R_2^*$  ( $1/T_2^*$ ) quantification. PDFF has been applied successfully in non-alcoholic steatohepatitis (NASH) drug trials and is increasingly used in clinical practice not least as a replacement for a liver biopsy (1). Beyond the liver, PDFF has been proposed as an imaging biomarker in the heart, muscle, pancreas, kidney, and adipose tissue deposits (2,3).  $R_2^*$  has shown utility in the quantification of liver iron content (LIC) (4).

The majority of advanced CSE algorithms, such as Iterative Decomposition of Water and Fat with Echo Asymmetry and Least-Squares Estimation (IDEAL) (5) and Variable Projection (VARPRO) (6), are complex-based, in the sense that they require both the MRI magnitude and phase images as input. Complex-based CSE estimates fat and water proportions indirectly through iterative estimation of  $B_0$  field inhomogeneity, conventionally referred to as the “field map”. Each field map value leads to a unique solution for water and fat proportions within a voxel (5–7). However, this implies dependence of water and fat estimation on accurate field map estimation. Importantly, field mapping is a nonconvex optimization problem with many local minima (7,8). Erroneous field map convergence leads to incorrect PDFF quantification, that may manifest as fat-water swaps in the PDFF images (7). Spatial smoothness constraints are often imposed on the field map to regularize the optimization, for instance through using region-growing (7,9), Markov Random Fields (MRF) (6), or graph cuts (8,10). These methods have been shown to work well in a range of conditions. However, the imposed smoothness constraints may be inappropriate, depending on the magnetic susceptibility of the object, or in transition regions with high field inhomogeneity, causing over-smoothing of PDFF and compromising any downstream quantitative measurements. Other limitations of such methods may include their sensitivity to initial seed pixels, which may also lead to incorrect PDFF values.

CSE methods that use only the magnitude of the MRI source images, which we refer to as magnitude-based, have also been proposed (11). Magnitude-based methods do not require field map estimation prior to water-fat separation and have been shown to be robust to errors in phase images due, for example, to eddy currents. In practice, complex-based methods are often subject to a final magnitude fitting step to correct phase errors in water and fat images, an approach that has been dubbed “hybrid” estimation (12). Magnitude-based methods optimize water and fat (and thus PDFF) directly but have tended to suffer from water-fat ambiguity, meaning they could not identify the dominant species within a voxel (water or fat), which, it was believed, limited the dynamic range of PDFF to 0 to 50% (1,11,13,14). A recently proposed method, MAGO (MAGnitude-Only), exploits the spectral complexity of fat to unambiguously identify the dominant species and thus generate estimates of PDFF over the entire 0-100% PDFF range (15). MAGO has been shown to give excellent accuracy and reproducibility across manufacturers and clinical field strengths, in simulations, phantoms and in-vivo

studies (15). Recently an extension to MAGO, MAGORINO, has been proposed, which accounts for the Rician noise distribution in magnitude-only MRI data and is reported to be more robust in low Signal-to-Noise Ratio (SNR) conditions, provided accurate noise characterization is performed (16).

Though field map estimation is not required for magnitude-based water-fat separation with full-range PDFF and accurate  $R2^*$  estimation, the field map may still be useful to assess image quality or, importantly, in the context of quantitative susceptibility mapping (QSM) (17). In QSM, the field map is subsequently decomposed into a local component and a background component. QSM has been successfully applied in the abdomen for measurement of liver iron content (17).

In this study, we show how MAGO may be extended to estimate the field map from complex-valued data following magnitude-based water-fat separation and PDFF estimation with resolved water-fat ambiguity. The advantages of our method are assessed using theory and simulations. Liver PDFF and field map values are compared to those calculated using state-of-the-art regularized complex-based implementations of field mapping in low field inhomogeneity regimes, using a cohort from the UK Biobank imaging sub-study. The methods are then compared under conditions of higher field inhomogeneities with rapid variation.

## Theory

### Signal Models

PDFF fitting conventionally uses the following generalized signal model at each pixel, which is not made explicit to simplify the notation:

$$s_n = (\rho_W + \rho_F C_n) e^{i(2\pi f_B t_n + \phi_0)} e^{-R_2^* t_n} \quad \text{Equation 1}$$

where  $s_n = s(t_n)$  is the observed signal at echo time  $t_n$ , where there are a total of  $N$  echoes  $[t_1, t_2, \dots, t_N]$ ,  $\rho_W$  is the unknown water magnitude and  $\rho_F$  is the unknown fat magnitude, and  $f_B$  is the frequency shift due to local field inhomogeneities or “field map” ( $2\pi f_B$  is sometimes expressed as  $\psi$ ). The term  $C_n = \sum_{p=1}^P \alpha_p e^{i2\pi f_p t_n}$  addresses the multi-frequency nature of the fat species, where  $\alpha_p$  and  $f_p$  are the relative amplitudes and relative frequencies of the spectral model of fat with  $P$  peaks, and it is assumed in this work that this is known a priori. We may for instance adopt the commonly used 6-peak liver model (18). This signal model is phase-constrained (19–21), meaning that water and fat share

the same initial phase  $\phi_W = \phi_F = \phi_0$ , which is a reasonable assumption in spoiled gradient echo acquisitions (22), and provides noise performance advantages (20).

When fitting only the magnitude of the signal, the model becomes

$$|s_n| = |\rho_W + \rho_F C_n| e^{-R_2^* t_n} \quad \text{Equation 2}$$

where  $|x|$  denotes the modulus. Note that the exponential term contributes only to the phase information,  $e^{i(2\pi f_B t_n + \phi_0)}$ , has unit modulus, and is dropped. It follows that magnitude-based methods avoid computing both the field map  $f_B$  and the initial phase term  $\phi_0$ . Finally, PDFF may be computed using the water and fat magnitudes using the ratio

$$\text{PDFF} = \frac{\rho_F}{\rho_W + \rho_F} \times 100 \text{ (\%)} \quad \text{Equation 3}$$

## Magnitude Fitting with Resolved Water-Fat Ambiguity

As noted above, prior to MAGO, magnitude methods had been limited to PDFF values in the range to 0-50%. It was shown recently that spectral complexity and multipoint optimization helps resolve the water-fat ambiguity, as reported with the MAGnitude-Only (MAGO) algorithm (15). MAGO is confounder-corrected for a composite fat spectrum,  $R_2^*$  bias, T1 bias, noise bias (23) and phase errors. The method enables full-range fat-fraction estimation and may be implemented independently at each voxel.

In MAGO, at each voxel the magnitude signal equation above is solved twice using nonlinear optimization from two different starting points, one near 0% PDFF, the other near 100% PDFF (15). For each of the two starting points, candidate solution sets  $\{\rho_W, \rho_F, R_2^*\}_1$  and  $\{\rho_W, \rho_F, R_2^*\}_2$  are obtained. The solution chosen by MAGO at each voxel,  $\{\rho_W, \rho_F, R_2^*\}$ , is the one with lower associated fitting residual. The ‘alternative’ MAGO solution will be chosen as the candidate solution set with the higher associated fitting residual, where fat and water will be ‘swapped’. This enables full-range PDFF estimation from 0% to 100%. The ‘alternative’ MAGO solution may be kept to further refine PDFF and  $R_2^*$ , as described in the next sections.

Figure 1 shows an illustration of the chosen MAGO solution set and the alternative MAGO solution set. The chosen solution set contains at each voxel the Water, Fat, PDFF and  $R_2^*$  values with lower associated fitting residual (better fit). The alternative solution set contains at each voxel the Water, Fat, PDFF and  $R_2^*$  values with higher associated fitting residual (worse fit).

## Proposed Voxel-Independent $B_0$ Field Estimation using Full-Range PDFF and $R2^*$

The chosen full-range magnitude-based solution set from MAGO,  $\{\rho_W, \rho_F, R_2^*\}$ , may be used to guide field map  $f_B$  (and initial phase  $\phi_0$ ) reconstruction using the input complex-valued data. To this end, we explore whether prior knowledge about water, fat and  $R_2^*$  may be useful for estimating the optimal field map at a given voxel.

For given values of water, fat and  $R_2^*$ , the following terms of the complex-based signal model in Equation 1 are known:  $q_n \equiv (\rho_W + \rho_F C_n)$  and  $R_n \equiv e^{-R_2^* t_n}$ , which may be rearranged to yield the simplified expression:

$$\frac{s_n}{q_n R_n} = e^{j(2\pi f_B t_n + \phi_0)}$$

This implies that the field map  $f_B$  and the phase offset  $\phi_0$  can be estimated given  $\rho_W$ ,  $\rho_F$ ,  $R_2^*$  and using the input complex-valued data  $s_n$ . Taking the phase from both sides,

$$P_n = \arg\left(\frac{s_n}{q_n R_n}\right) = 2\pi f_B t_n + \phi_0 + 2\pi k \quad \text{Equation 4}$$

with  $k$  an integer, then the estimation may be formulated as a linear equation in matrix form,

$$\mathbf{P} = \begin{bmatrix} P_1 \\ \vdots \\ P_N \end{bmatrix} = \begin{bmatrix} 2\pi t_1 & 1 \\ \vdots & \vdots \\ 2\pi t_N & 1 \end{bmatrix} \begin{bmatrix} f_B \\ \phi_0 \end{bmatrix} = \mathbf{A} \boldsymbol{\varphi} \quad \text{Equation 5}$$

where  $\boldsymbol{\varphi} = [f_B, \phi_0]^T$  are unknowns, and  $\mathbf{A}$  is a  $N \times 2$  matrix where the first column vector contains the echo times and the  $2\pi$  term,  $[2\pi t_1, 2\pi t_2, \dots, 2\pi t_N]^T$ , and the second column contains ones  $[1, 1, \dots, 1]^T$ . This makes for a computationally efficient estimation.

For each pixel in the source image, the proposed algorithm first creates the  $q_n$  and  $R_n$  terms using the MAGO chosen solution set  $\{\rho_W, \rho_F, R_2^*\}$ , the echo times and the given spectral model of fat. The 6-peak liver model was used in this work (18). Then, the input complex-valued data  $s_n$  is divided by the  $q_n R_n$  term,  $s_n/(q_n R_n)$ . The phase of the output is taken and unwrapped in the *echo times' dimension* (rather than in the spatial dimensions), by changing absolute jumps greater than  $\pi$  to their  $2\pi$  complement

starting from the first echo time. The echo times' matrix  $\mathbf{A}$  is then defined and used to find a least squares solution to the linear equation system in Equation 5.

For correction in the presence of bipolar gradients that create an additional phase shift to the signal  $(-1)^n \theta$  (24), one may reformulate Equation 5 to estimate three unknowns,  $\boldsymbol{\varphi}' = [f_B, \phi_0 - \theta, \phi_0 + \theta]^T$ , namely the combination of the common phase offset of water and fat,  $\phi_0$ , and a phase offset due to bipolar gradient effects,  $\theta$ , with opposite sign for odd and even echoes. In this scenario, the echo times matrix  $\mathbf{A}'$  may be defined as a  $N \times 3$  matrix as follows (for even  $N$ ):

$$\mathbf{A} = \begin{pmatrix} 2\pi t_1 & 1 & 0 \\ 2\pi t_2 & 0 & 1 \\ \vdots & \vdots & \vdots \\ 2\pi t_N & 0 & 1 \end{pmatrix}$$

This approach enables parameter sharing of the bipolar gradients term and the initial phase offset, which may be disentangled further into  $\phi_0$  and  $\theta$ . Disentangling into  $\phi_0$  and  $\theta$  was out of the scope of this work as these two terms are often considered unimportant (19).

We may additionally estimate  $f_B$  and  $\phi_0$  using this approach for the MAGO *alternative* solution set as well, which may provide a basis to refine the MAGO PDFF and  $R_2^*$  maps. One proposed implementation of such refinement is described in the Methods section.

## B<sub>0</sub> Field Cost Function: $R(f_B)$

The overall residual of the signal model may be plotted against the field map, for visual assessment of the cost (or loss) function  $R(f_B)$  (7–9). For voxel-independent iterative complex-based estimation, for instance the IDEAL approach (5) with  $R_2^*$  decay and multi-peak fat spectrum modelling (25), the field map  $f_B$  may be estimated by minimizing the residual loss function  $R_C(f_B)$ :

$$R_C(f_B) = \|[R_1, R_2, \dots, R_N]\|_2^2 = \sum_{n=1}^N (s_n - \hat{s}_n)^2$$

where  $\hat{s}_n$  is the noiseless signal equation using the estimated values  $\{\widehat{\rho}_W, \widehat{\rho}_F, \widehat{f}_B, \widehat{R}_2^*\}$ . For our proposed estimation method, where full-range magnitude-based estimates are used as inputs, the residual loss function to minimize is based on Equation 5:

$$R_M(f_B) = \|\mathbf{P} - \mathbf{A} \boldsymbol{\varphi}\|_2^2$$

Figure 2 plots the cost functions for the complex-based formulation,  $R_C(f_B)$ , and for our proposed formulation,  $R_M(f_B)$ , within a voxel; the former replicates Figure 1a from Yu et al (7), but with the addition of  $R_2^*$  decay, 6-peak fat spectrum modelling (18), and evenly spaced echo times (3 echoes,  $TE_1=2$  ms,  $\Delta TE=2$  ms). For the particular case of uniformly spaced echo times, the cost function is periodic with period  $1/\Delta TE$  (8,9). The loss function curves were simulated over the field map range -1000 to 1000 Hz at 1.5 T (imaging frequency = 64 MHz), using the true values of water, fat and  $R_2^*$ . The cost functions were plotted for varying water:fat proportions, namely 4:1, 2:1, 1:1, and 1:2.

Voxel-independent IDEAL estimation wrongly converges to a local minimum ('aliased' solution) when the true field map value is beyond approximately  $\pm \Delta f/2$ , where  $\Delta f$  is the off-resonance frequency of the main fat peak relative to water ( $\Delta f \approx 220$  Hz at 1.5 T), as described previously (7,8). The voxel-independent VARPRO implementation has been reported to produce equivalent results to voxel-independent IDEAL, because ambiguities are dealt with by forcing the field map to be within  $\pm \Delta f/2$  (8). Such erroneous convergence may lead to fat-water swapping in the PDF map (7,14).

Conversely, the field mapping method proposed here converges to the correct value with starting estimates beyond the  $\pm \Delta f/2$  range for the same simulated raw data. Note that our formulation reduces the number of local minima in the search space compared to complex-based field mapping methodologies such as IDEAL. In addition, field mapping with the proposed formulation is independent of water:fat proportion, because prior water and fat estimation from unambiguous magnitude-based fitting followed by demodulation of the water and fat signal term from the observed complex-valued source data removes the local minima associated with the water-fat phase shift.

## Methods

### MRI Data

N=152 nominally healthy UK Biobank ([www.ukbiobank.ac.uk](http://www.ukbiobank.ac.uk)) volunteers were gathered, each of whom had been scanned using a Siemens Magnetom Aera 1.5 T scanner (Siemens Healthineers, Erlangen, Germany) and following a two-dimensional single-slice, 10 mm slice thickness, 6-echo ( $TE_1=1.2$  ms,  $\Delta TE=2$  ms) gradient-recalled echo (GRE) protocol designed to minimize T1 bias ( $5^\circ$  flip angle). UK Biobank is approved by the North West Multi-Centre Research Ethics Committee, and prior written consent was obtained from all participants.

One other dataset was gathered using a Siemens Prisma 3 T scanner on a healthy volunteer to test the method under high field inhomogeneities. Informed consent was obtained from the participant. The



acquisition comprised thirty-two slices including the dome of the liver, heart, and lungs. The acquisition consisted of a 6-echo ( $TE_1=1.3$  ms,  $\Delta TE=1$  ms) gradient-recalled echo (GRE) protocol designed to minimize T1 bias ( $3^\circ$  flip angle), Pixel Bandwidth = 1565 Hz, and  $232 \times 256$  reconstructed image size, with 5 mm slice thickness and  $1.72 \times 1.72$  mm<sup>2</sup> in-plane resolution. This scan represented a challenging example for comparing the proposed method with state-of-the-art complex-based methods, due to the high field inhomogeneity range across the image and through the slices.

## Overview of the Proposed Methodology

An overview of the proposed methodology is shown in Figure 3 and visually compared with state-of-the-art complex-based (hybrid) water-fat separation pipelines. In current approaches, field map estimation, and therefore PDFF estimation, can only be carried out when complex data is available, which may be challenging in clinical settings and/or for particular makes and models of MRI scanners. Starting with complex-valued source data, these methods start by field mapping with some regularization (e.g., region-growing, graph cuts). The field map then yields unique Water, Fat and  $R_2^*$  maps, which may then be used as starting maps for a magnitude-based refinement step.

In our method, PDFF estimation is possible regardless of whether phase data is available or reliable. When phase data is available and (sufficiently) reliable, our voxel-independent field mapping methodology may be run. Then, the field map may be adjusted, which yields refined magnitude-based PDFF and  $R_2^*$  estimates.

The proposed adjustment of the field map, that enables the refinement of the PDFF and  $R_2^*$  maps from MAGO, is described in the next section.

## Proposed Adjustment of Voxel-Independent Field Map and PDFF and $R_2^*$

To this point, the proposed method may run independently at each voxel. This is referred to as the *proposed voxel-independent field mapping* throughout this work and is subsequently used in simulation experiments. Further to that, an MRI physics-inspired adjustment of the voxel-independent field map may be performed, which then allows the refinement of the MAGO PDFF and  $R_2^*$  estimated maps. This is possible once the voxel-independent field maps for both the chosen MAGO solution set and the alternative MAGO solution set have been computed using the *proposed voxel-independent field mapping* method.

An adjusted field map may be created by selecting at each voxel the candidate solution set (chosen set or alternative set) with an associated field map value that is closest to a smoothed version of the field map derived from the *chosen* MAGO solution. This step yields a postprocessed field map as well as postprocessed or ‘refined’ PDFF and  $R_2^*$  maps, because the whole solution set is consistently kept.

In one proposed example of this approach, median filtering with kernel size of 15-by-15 neighborhood is initially used on the chosen field map to create a spatially smooth field map. Then, the field map values in the solution sets (chosen and alternative) are compared to that smooth field map. If the field map value from the alternative solution set is closer to the smooth field map than the field map from the chosen solution set, then the chosen and alternative solution sets are interchanged for that voxel. In other words, if the absolute difference between the chosen field and the smooth field is higher than the absolute difference between the alternative field and the smooth field, then the chosen and alternative solution sets are interchanged.

This adjustment step was tested under low SNR conditions using simulations, as described in the next section. The 3 T dataset was run with the *proposed voxel-independent field mapping* method and with the *proposed adjusted field mapping* method, the latter using the proposed adjustment step described here.

## Simulations

In one simulation a slowly-varying synthetic field map was added to one UK Biobank subject to further explore the observation from the Theory section, illustrated in Figure 2. The water magnitude, fat magnitude, and  $R_2^*$  from region-growing IDEAL fitting (7) were used as reference to synthesize complex-valued echo images with our additional synthetic field map and synthetic initial phase offset. The initial phase was set to  $\pi/4$  rad for the whole image. The synthetic field map was set to vary linearly, starting from the center of the image, and including (and exceeding) field inhomogeneities of  $\pm\Delta f$ . The same echo times of the original UK Biobank dataset were used in the simulation, and the 6-peak fat spectral model was used to generate the synthetic data. The synthesized complex-valued echo data was reconstructed with voxel-independent IDEAL, as well as voxel-independent MAGO water, fat and  $R_2^*$  estimation followed by the proposed voxel-independent implementation of our method.

One other simulation was performed to test the performance of the proposed adjustment of the field map at the refinement of the magnitude-based PDFF and  $R_2^*$  maps, in normal SNR and low SNR conditions. One UK Biobank subject was used for the simulation. The Signal-to-Noise Ratio (SNR) of the dataset was measured from the image background. PDFF and field map estimation was performed without any additional noise using 1. The voxel-independent implementation of the proposed field

mapping methodology, and 2. The proposed method with the field map adjustment and PDFF and R2\* refinement step. Complex Gaussian noise was then added to the source data to bring SNR down to 5, and PDFF and field map were estimated again using the voxel-independent implementation of our method and the implementation with adjustment.

## In-Vivo Evaluation

The voxel-independent implementation of our method as well as the implementation of our method with adjustment were compared against implementations of state-of-the-art complex-based methodology in UK Biobank and the thirty-two-slice dataset.

The 152 UK Biobank subjects were used to validate the proposed methodology for *in vivo* agreement with state-of-the-art complex-based methodology under low  $B_0$  field inhomogeneities. The UK Biobank subjects were processed using a previously validated Hybrid T2\*-IDEAL implementation, consisting of the T2\*-IDEAL method with an additional refinement step using magnitude fitting, and including field mapping regularization using the region-growing algorithm proposed by Yu et al. (7,12,26,27) and the 6-peak spectral model of fat reported in liver (18). The field maps and PDFF maps resulting from this method were used as reference. The subjects were also processed using the voxel-independent (or voxel-wise) implementation of our proposed method. Median PDFF and field map values of the Hybrid IDEAL and our proposed methodologies were extracted within automatically defined liver segmentation masks, that were obtained using a previously trained deep learning-based liver segmentation model (28). The methods were compared for field map and PDFF agreement using Bland-Altman analysis (29).

The thirty-two-slice 3 T dataset was used to compare our proposed implementations with three widely used complex-based implementations in the literature. The three complex-based implementations performed field mapping with regularization using the following methods: Region Growing (RG) (7), Graph Cuts (GC) (8), and Phase Regularized Estimation using Smoothing and Constrained Optimization (PRESCO) (19). In order to obtain PDFF maps from these methods, their outputted field maps were used to initialize the same implementation of Hybrid IDEAL used on the UK Biobank subjects, because this implementation allowed for the inclusion of a bipolar gradients' correction step from Peterson et al. (30). This in turn yielded the following PDFF estimation methods: *RG-IDEAL*, *GC-IDEAL*, and *PRESCO-IDEAL*, respectively, where RG-IDEAL means Hybrid IDEAL initialized with the RG output field map, etc.

The implementation of GC from the Fat-Water Toolbox (<http://ismrm.org/workshops/FatWater12/data.htm>) was used with the default parameters, except for

the field map search range which was doubled to [-800, 800] Hz. The implementation of PRESCO available online (<https://github.com/marcous/pdf>) was used with the default parameters.

The field maps and PDFF maps from RG, GC and PRESCO were compared with those generated from the voxel-independent as well as the adjusted field map implementation of our method. Correction for bipolar gradients was also run for our methods, using the approach explained in the Theory section.

## Results

### Simulations

Figure 4 shows the UK Biobank subject with the additional synthetic field map, reconstructed using the voxel-wise IDEAL method and with the voxel-wise implementation of our method. In accordance with the observations from Figure 2, the voxel-independent IDEAL method erroneously converges to an aliased solution beyond an initial field map value that is beyond the true field  $\pm\Delta f/2$  (with  $\Delta f \approx 220$  Hz at 1.5T). This results in fat-water swaps in the PDFF map. Consistently with Figure 2 also, the voxel-independent implementation of the proposed field mapping method enables estimation of field map beyond the  $\pm\Delta f/2$  range, up to slightly beyond  $\pm\Delta f$ .

Figure 5 shows the proposed refinement of MAGO PDFF ( $R_2^*$  not shown) on a UK Biobank subject, following the field map adjustment step, starting from the voxel-independent field map derived from the chosen MAGO solution and the voxel-independent field map derived from the alternative MAGO solution. For a measured SNR of 23, the postprocessing step shows refinement of a few pixels near edges of structures, but overall, modest improvement in map quality over the voxel-independent MAGO result. Figure 6 shows the proposed refinement for a simulated SNR of 5, after the addition of complex noise to the raw data. The adjustment step was able to fix or ‘unswap’ many pixels, importantly within the liver, and render a solution that is comparable to the reference PDFF map from the high SNR case.

### In-Vivo Evaluation

Figure 7 shows Bland-Altman comparisons of median PDFF and median field map values within the liver for the RG-IDEAL implementation and our method, using the UK Biobank subject population. For PDFF quantification, a small bias of -0.02 % PDFF and low variability [-0.1, 0.1] % PDFF were observed, with overall excellent agreement of the RG-IDEAL algorithm and our method for PDFF. For Field map quantification, a small bias of -0.05 Hz and low variability [-0.2, 0.3] Hz were observed, with overall excellent agreement of RG-IDEAL and our method.

Figure 8 shows one subject from the UK Biobank for three reconstruction methods: voxel-independent IDEAL, RG-IDEAL and the MAGO estimation (15) followed by our proposed field mapping method. Note that, for the proposed approach, and contrarily to the other two methods, field mapping follows PDFF estimation, rather than the opposite. As can be observed, the proposed field mapping method produces results that are comparable to the RG-IDEAL algorithm, whereas the voxel-independent IDEAL estimation suffers from field map aliasing posteriorly in the liver, part of the subcutaneous fat and near the spleen region. Inaccurate field map estimation results in consequent fat-water swaps on the PDFF map, including a ‘double-swap’ within the liver. Double swaps are those which result in reasonable PDFF values, which may lead to misdiagnosis if not properly identified (7).

Figure 9 and Figure 10 show six of the thirty-two slices from the 3 T dataset that contain the liver but are distanced from the isocenter. Magnitude images from the first echo time are provided alongside for anatomical reference. The case shows both high field inhomogeneities overall as well as rapid field variations near edges of organ structures, for example the dome of the liver or the spleen. Though there are no ground truth field maps or PDFF maps available, the slice-by-slice variation in the field map as well as in PDFF is expected to be consistent. The slice-by-slice increase in the field maps and PDFF maps by the proposed ‘voxel-wise’ and ‘adjusted’ methods is consistent, whereas the other methods converged to incorrect values at some distance from the isocenter, for at least one organ structure. The PRESCO method (19) showed agreement with the proposed method in most regions but showed erroneous convergence in and around the spleen region for one slice. The proposed ‘voxel-wise’ method presented some sensitivity to noise and erroneous convergence in some regions of the subcutaneous fat, that were corrected with the proposed ‘adjusted’ method. Note that no information from neighboring slices was used for any of the methods.

In Figure 10, PDFF maps for the complex field mapping methodology were affected where the field maps in Figure 10 had converged incorrectly. PDFF maps were affected by fat-water swapping in all but the proposed field mapping method. Note that PDFF for the proposed methodology is computed first from the magnitude data using MAGO, so that, even if the field map was affected (for instance, by values beyond  $\pm\Delta f$ ), the PDFF values would be unchanged.

## Discussion

$B_0$  field mapping, while important for image quality assessment and quantitative susceptibility mapping (QSM) applications, need not be a critical step for correct water-fat separation. Our results demonstrate the feasibility of field mapping after magnitude-based water-fat separation with resolved water-fat ambiguity (MAGO). The proposed PDFF estimation and field mapping were comparable to regularized

state-of-the-art complex-based reconstruction in simulated data and in subjects from the UK Biobank sub-study. Our method showed robustness in regimes with high field inhomogeneities, including rapid spatial variation of the field map near abdominal structures such as the liver and the spleen.

The PDFF and  $R_2^*$  maps, which are the parameters of interest, produced by our method are initially magnitude-based with resolved water-fat ambiguity. The field map is a separate parameter that may be estimated more robustly once PDFF and  $R_2^*$  have been estimated, provided phase information is available and error-free. We showed that local minima associated with the phase shift due to the off-resonance frequency of fat are removed when using the proposed method, via demodulation of the water and fat component from the complex-valued raw data. For scanners where obtaining reliable phase images is a challenge, our method still enables robust PDFF and  $R_2^*$  estimation. For this reason, our method may be more easily standardized and robustly deployed across a range of scanning conditions. Indeed, our methodology may be applied to the routinely observed SNR levels of 6- and 12-echo datasets in both 1.5T and 3T research and clinical scanners. Examples of 1.5 T and 3 T were provided within this work, though a more extensive 3T exploration needs to be carried out in the future. Noise performance analysis was outside the scope of this paper –though we tested the robustness of the field map adjustment step in simulated low SNR = 5– and needs to be carried out in future work.

Field map regularization in complex-based estimation, notably due to incorrect smoothness assumptions, may propagate wrong field map and PDFF values to the entire organ of interest (e.g. liver or pancreas). This is especially important for methods that are sensitive to initial estimations, for instance on seed pixels in down-sampled data (7,9). This may be the case in slices that are distanced from the isocenter within multi-slice acquisitions, where field inhomogeneity tends to be high. An example dataset at 3T illustrated this effect, whereas the proposed method produced robust field maps over the range of observed field inhomogeneity (exceeding 300 Hz), which were achieved by using the previously estimated water and fat values. This suggests that the MAGO approach is more robust than complex- or hybrid-based methods, where correct PDFF estimation critically depends on correct field map convergence.

While the proposed field map adjustment step may be considered a form of spatial regularization, note that the proposed method is subtly distinct: instead of (over-)smoothing the field map directly, the postprocessed field map at a given voxel comes from the choice of one of the two pre-computed candidate MAGO solution sets (chosen set or alternative set). Thus, the field map value at a given voxel is derived directly from that voxel’s complex-valued raw data, but it is chosen considering the information from the voxel neighborhood. This may avoid issues with previously presented spatial regularization methods, where the field map at a given voxel is forced to assume a value within a pre-defined range, given a combination of field map values from the voxel neighborhood, for example in the interpolation step of region growing (7). Our approach of choosing only from the two candidate

MAGO solutions did not penalize neighboring regions with rapid field variations, as other field mapping methods showed, and preserved the high-frequency appearance of the field map, whereas other methods yielded field maps with an over-smoothed appearance. In our implementation, a median-filtered version of the chosen field map was used to guide the field map adjustment step; other piece-wise techniques such as anisotropic diffusion may be considered in the future.

Note that our adjustment step may lead to a chosen MAGO solution set that is not necessarily associated with the lower fitting residual; instead, it is the solution with higher consistency with the voxel neighborhood. This may be useful in cases where noise or perturbations corrupt the raw data magnitude, causing the physiologically correct solution to become a local optimum, rather than the global optimum. For the refinement of the PDFF and  $R_2^*$  estimates, one could have alternatively chosen to use the adjusted field maps to directly compute updated water and fat proportions using the linearized IDEAL formulation. This would be undesirable as it could propagate phase errors, which would in turn need a magnitude-refining step. This is the same reasoning behind hybrid fitting (12). Again, choosing from only the two candidate magnitude-based solutions removes the need for a final magnitude fitting step present in hybrid methods.

Field map regularization techniques may be used to regularize the MAGO field map beyond the observed limit. For multi-slice acquisitions, recent work has proposed to impose smoothness constraints in the three dimensions for high field cases (8,31), which may also be incorporated for the challenging example shown in this work. The alternative of regularizing the phase offset map  $\phi_0$ , instead of the field map, has also been used, since the phase offset map is considered unimportant clinically (19). This could also help to preserve the local field map variation, where obtaining local susceptibility maps is of interest for QSM or other downstream applications.

## Conclusion

Our results suggest that magnitude-based water, fat and  $R_2^*$  estimation with resolved water-fat ambiguity may be used to robustly estimate a field map from complex-valued raw data. This approach for water-fat separation and field mapping is robust and widely applicable, compared to complex- and hybrid-based approaches, which estimate the field map first and therefore rely on the availability and reliability of phase images.

## Figures

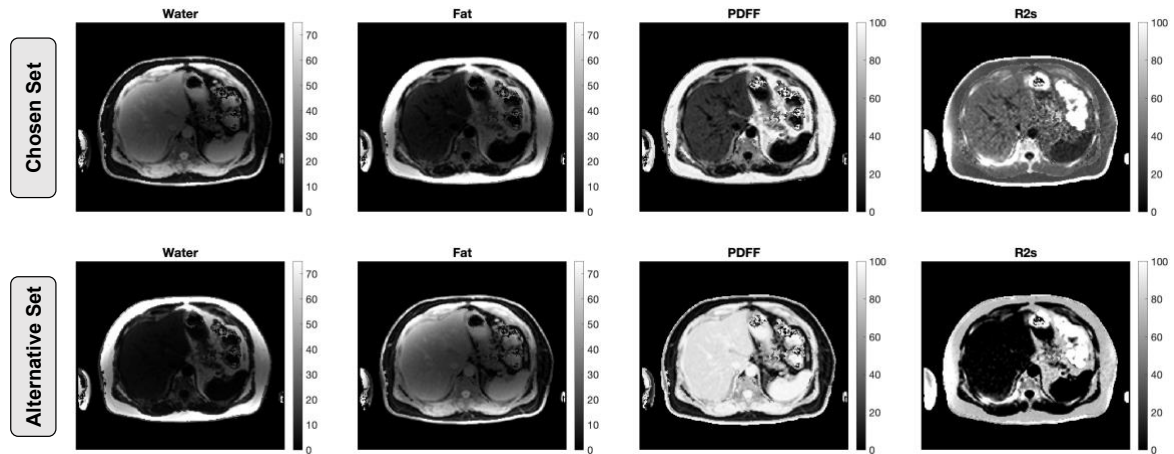


Figure 1. Illustration of magnitude fitting with resolved water-fat ambiguity (MAGO). MAGO uses multipoint search to converge to two solution sets, the water-dominant set and the fat-dominant set. Then chooses, for each pixel, the solution that fits best to the data using the residuals, leading to a chosen solution set (top row) and an alternative solution set (bottom row). This enables PDFF estimation over the full range (0 to 100%) as well as correct R2\* estimation for the fat-dominant voxels.



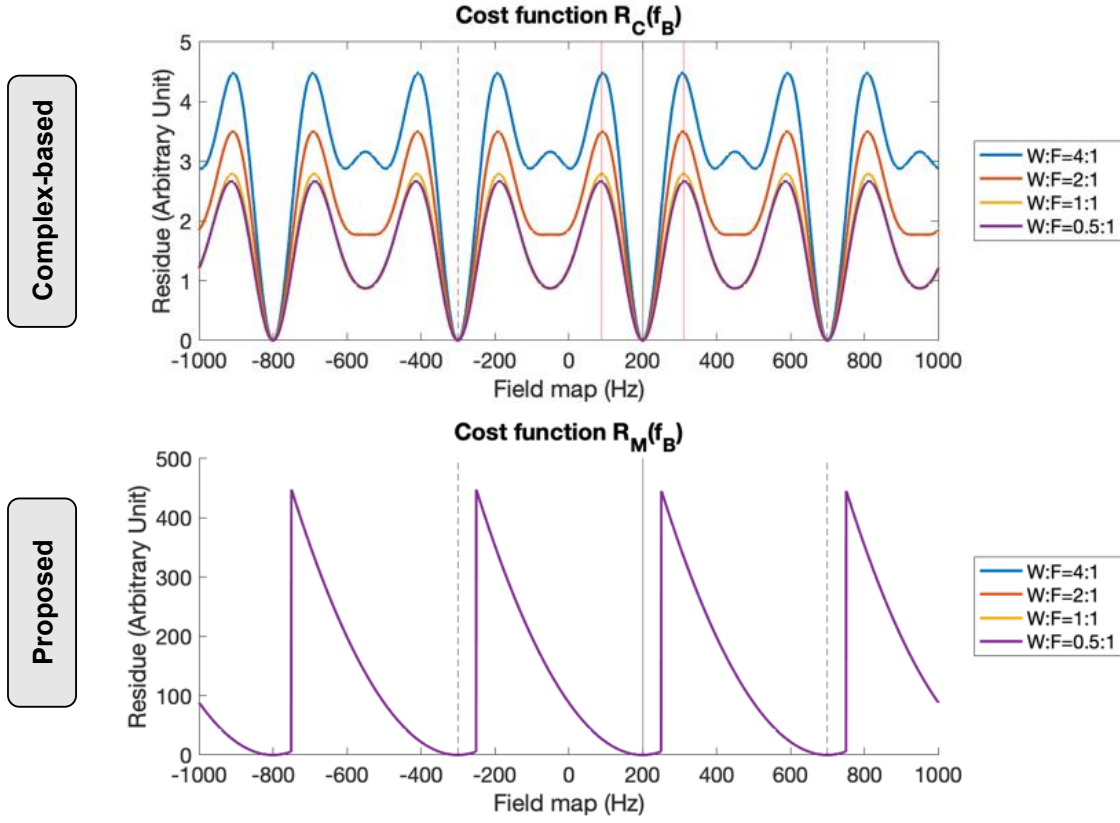


Figure 2. Simulated loss functions for the complex-based estimation problem (top) and for the proposed formulation (bottom) within a voxel. True field map = 200 Hz, varying voxel Water:Fat proportion,  $R_2^* = 30$  Hz,  $\phi_0 = 0$  rad. Three-echo dataset [2, 4, 6] ms, 1.5 Tesla, 6-peak liver fat spectrum. Iterative complex-based estimation with no regularization, for instance the IDEAL algorithm, converges to an incorrect local minimum near 0 Hz, whereas the proposed method converges to the true solution. The proposed loss function is also independent of the Water:Fat proportion. True solution is marked with a solid vertical grey line. The period of the loss function,  $\pm 1/\Delta TE$ , is marked (dashed lines), and true solution  $\pm \Delta f/2$  are marked in the top plot (red vertical line).

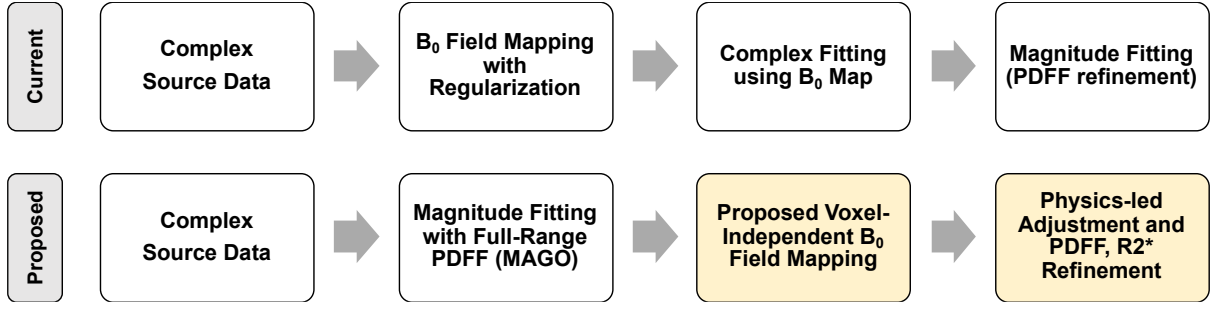


Figure 3. The state-of-the-art (top row) and the proposed (bottom row) methodologies for field mapping and PDFF estimation, given complex-valued source data. The yellow modules are described in this work. The state-of-the-art methodology performs field mapping with regularization first, and then derives PDFF and R2\*, with a final magnitude-based refinement step. The proposed methodology applies magnitude fitting with resolved water-fat ambiguity (MAGO) first, then performs voxel-independent field mapping, and posteriorly refines the magnitude-based PDFF and R2\* maps through a field map adjustment step.

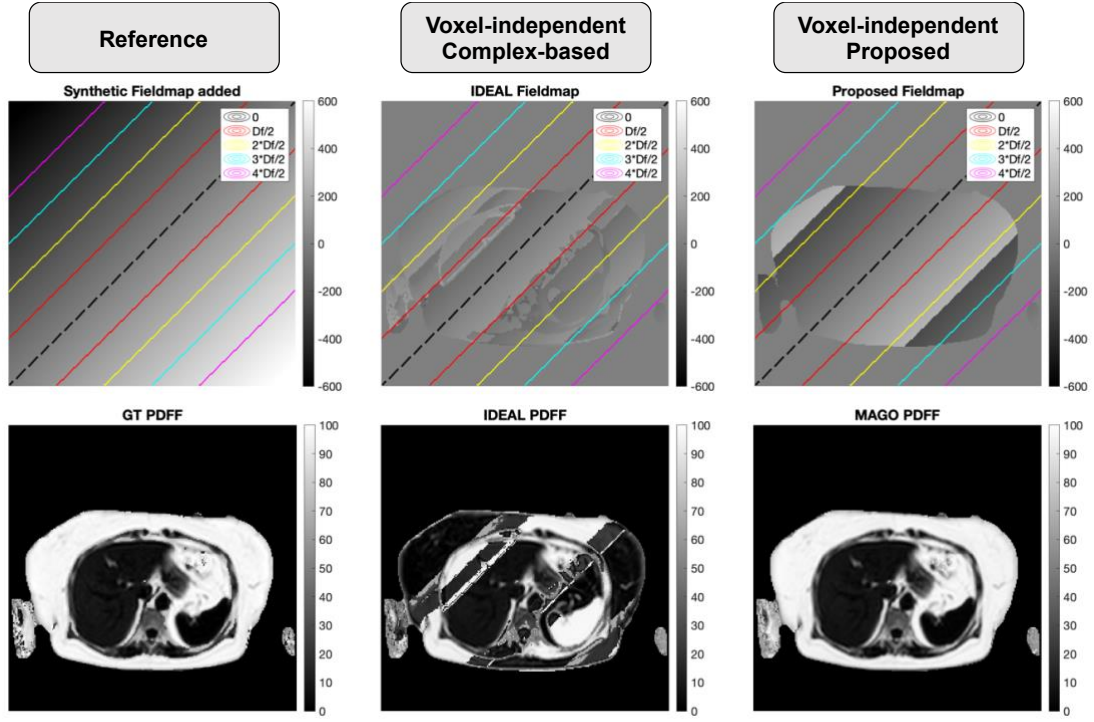


Figure 4. UK Biobank subject with a slowly-varying synthetic field map added. The reference PDFF comes from regularized complex-based estimation using region-growing IDEAL (left). Multiples of  $\pm\Delta f$  have been indicated (color lines). Voxel-independent IDEAL struggles beyond  $\pm\Delta f/2$ . The voxel-independent implementation of the proposed method extends the range of accurate field map estimation, up until  $\pm\Delta f$ .

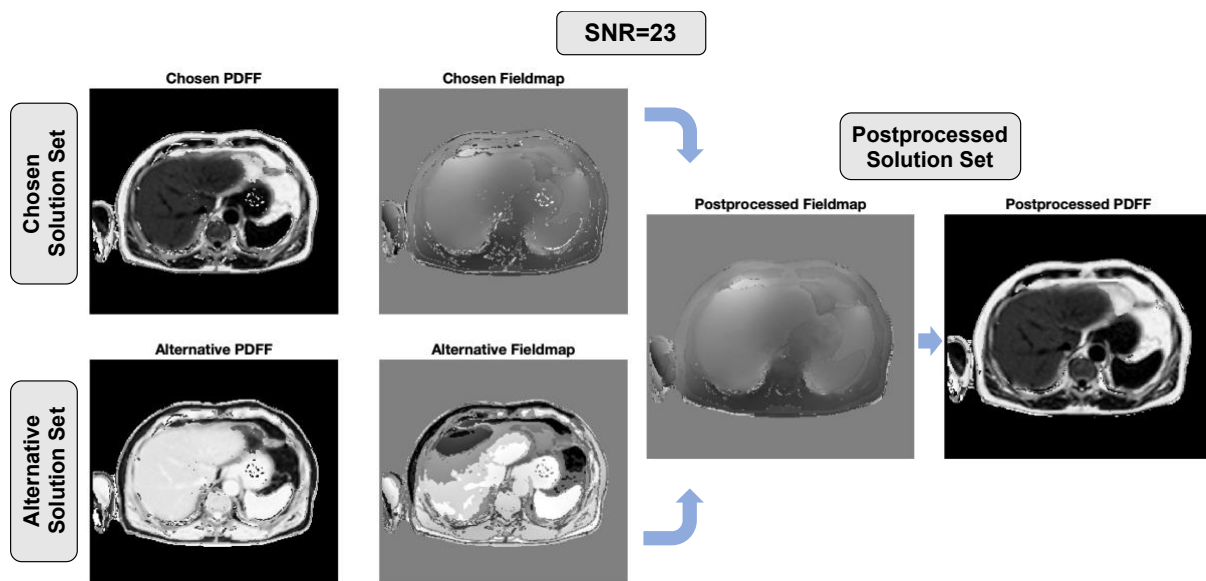


Figure 5. Refinement of the magnitude solutions using field map on a UK Biobank subject (SNR=23).

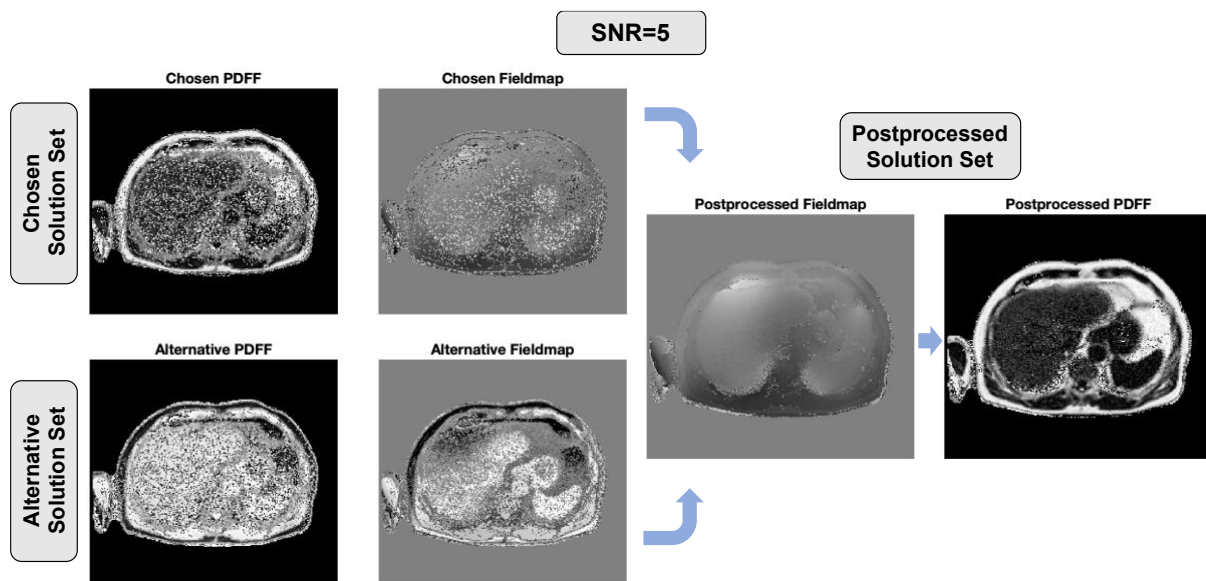


Figure 6. Refinement of the magnitude solutions using field map on a UK Biobank subject (SNR=5).

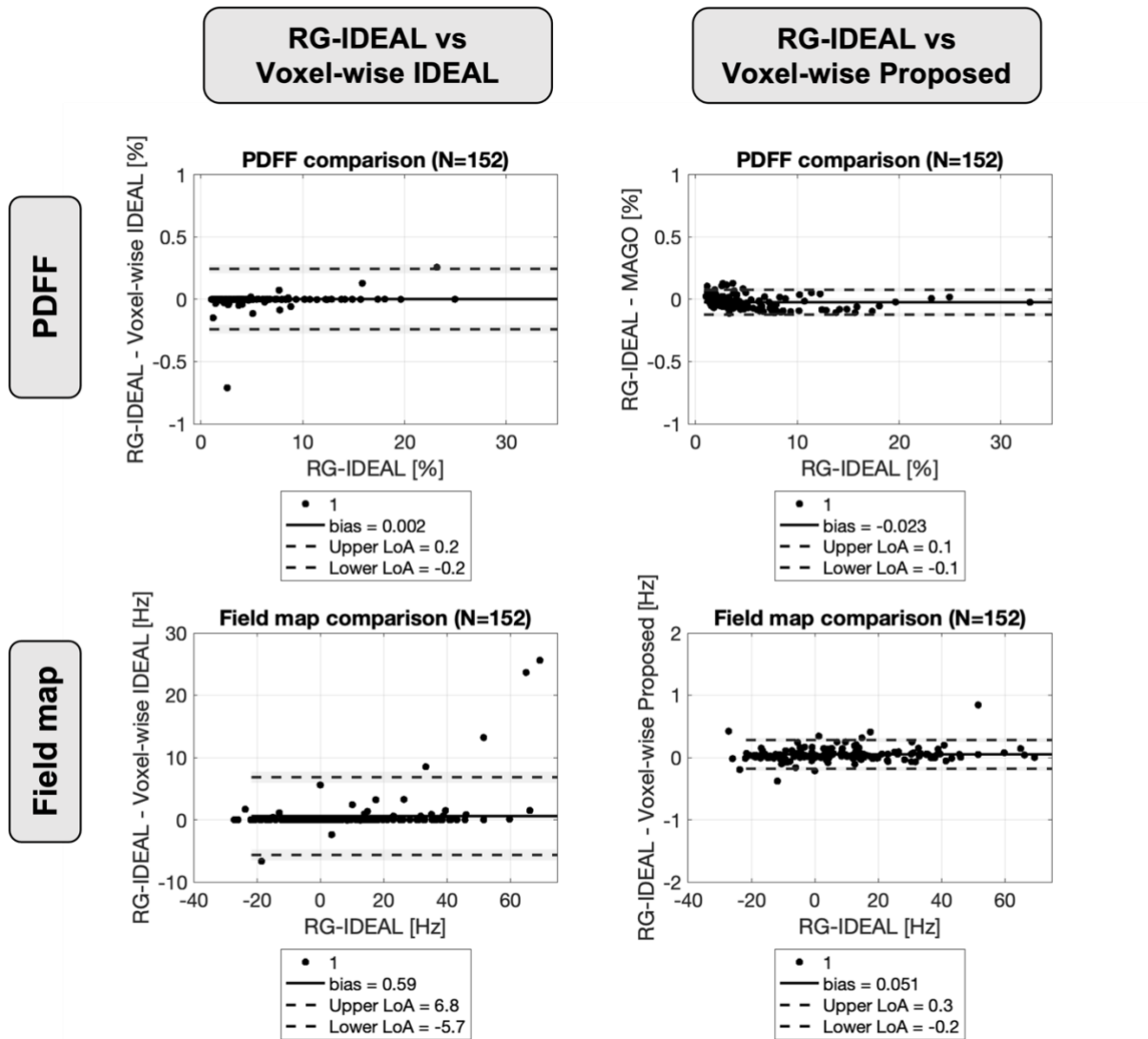


Figure 7. Bland-Altman comparisons of regularized complex-based estimation and the proposed regularized magnitude-based estimation on UK Biobank (1.5T) examples. PDFF (left) and Field map (right) values within liver segmentations were extracted. The methods show agreement for this cohort, which does not tend to suffer from high field inhomogeneities.

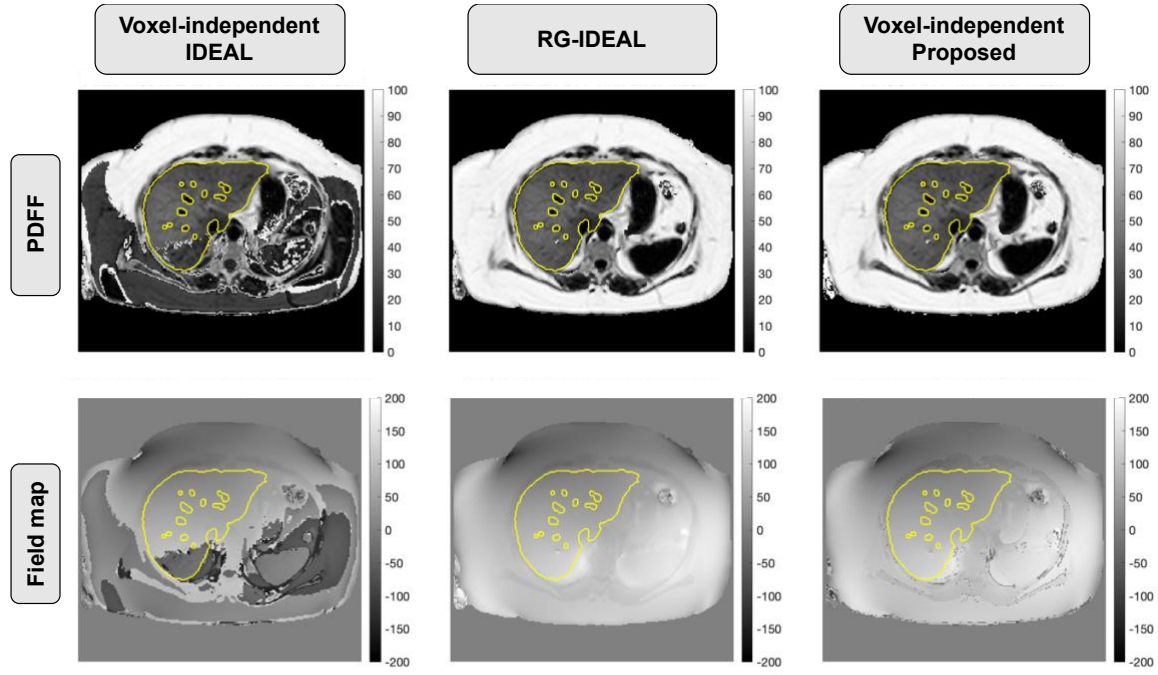


Figure 8. Subject from UK Biobank (Siemens Aera, 1.5T) showing overlaid automatic liver segmentations. Voxel-independent Hybrid IDEAL (this is, without region-growing initialization) (left), region-growing Hybrid IDEAL (RG-IDEAL) (middle), and MAGO with the proposed voxel-independent field mapping method (right) are shown. Note that, for the proposed method, field mapping follows PDFF estimation, contrarily to the complex-based methods compared.



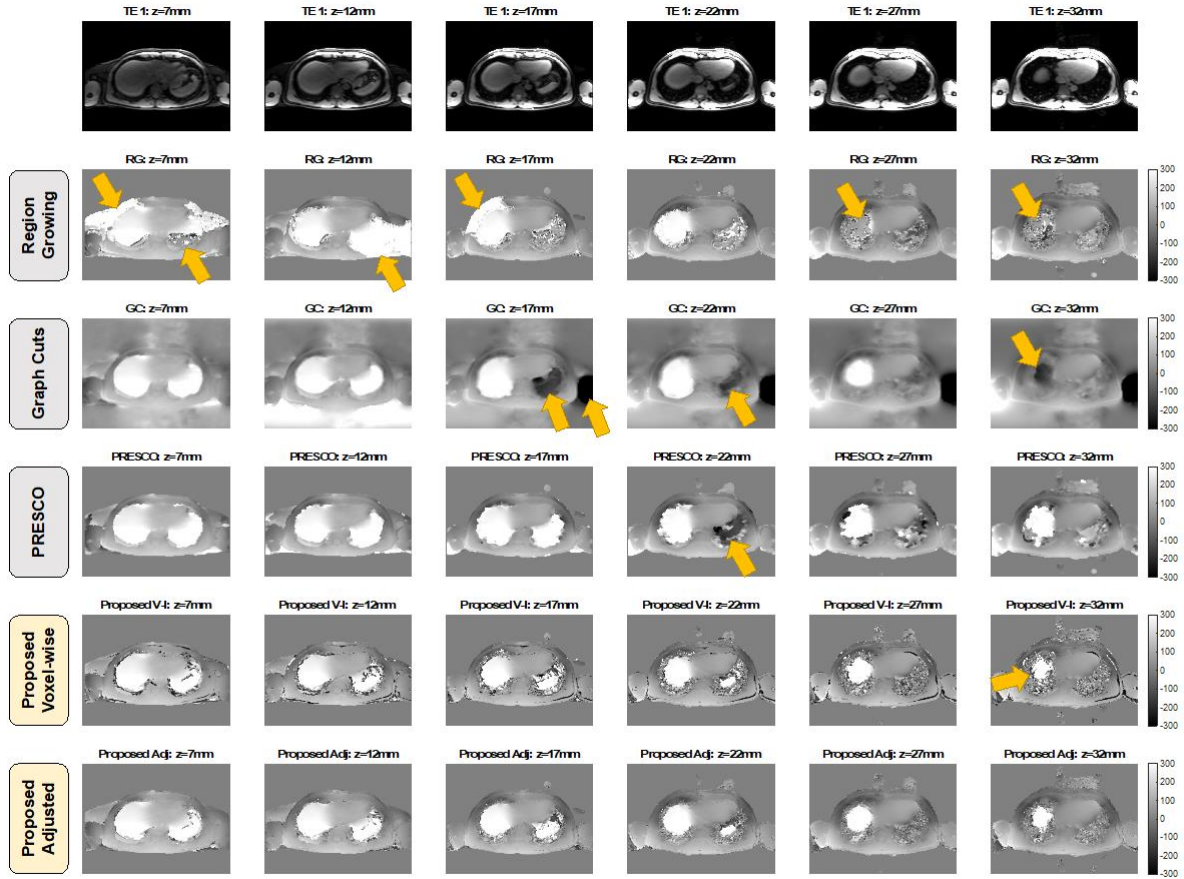


Figure 9. Field maps of six of the thirty-two slices from the 3 T dataset, processed with Region Growing, Golden Section Search, Graph Cuts, PRESCO and the proposed method. Magnitude images from the first echo time are provided for anatomical reference. Regions of high field inhomogeneity are observed, which should be consistent across contiguous slices. Regions of rapid spatial field variation are also observed, especially near the dome of the liver and in the spleen. Areas of field map convergence errors are indicated (arrows).

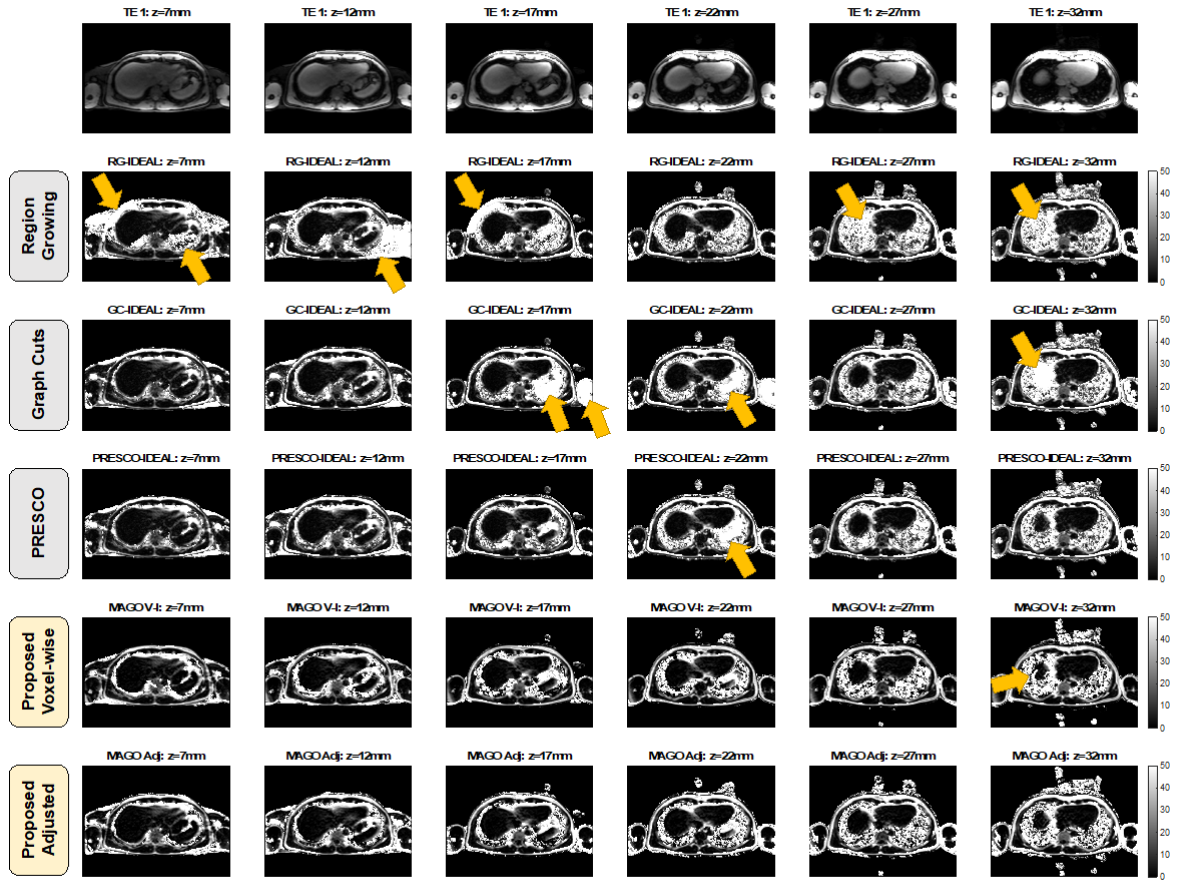


Figure 10. PDFF maps of six of the thirty-two slices from the 3 T dataset, processed with Region Growing, Golden Section Search, Graph Cuts, PRESCO followed by IDEAL, and the proposed method. Magnitude images from the first echo time are provided for anatomical reference. Fat-water swaps are observed where the field maps in Figure 9 showed incorrect convergence. Areas of fat-water swapping due to field map convergence errors are indicated (arrows).



## References

1. Caussy C, Reeder SB, Sirlin CB, Loomba R. Noninvasive, Quantitative Assessment of Liver Fat by MRI-PDFF as an Endpoint in NASH Trials. *Hepatology* 2018;68:763–772 doi: 10.1002/hep.29797.
2. Franz D, Diefenbach MN, Treibel F, et al. Differentiating supraclavicular from gluteal adipose tissue based on simultaneous PDFF and T2\* mapping using a 20-echo gradient-echo acquisition. *Journal of Magnetic Resonance Imaging* 2019;50:424–434 doi: 10.1002/jmri.26661.
3. Idilman IS, Tuzun A, Savas B, et al. Quantification of liver, pancreas, kidney, and vertebral body MRI-PDFF in non-alcoholic fatty liver disease. *Abdominal Imaging* 2015;40:1512–1519 doi: 10.1007/s00261-015-0385-0.
4. Hernando D, Levin YS, Sirlin CB, Reeder SB. Quantification of liver iron with MRI: State of the art and remaining challenges. *Journal of Magnetic Resonance Imaging* 2014;40:1003–1021 doi: 10.1002/jmri.24584.
5. Reeder SB, Wen Z, Yu H, et al. Multicoil Dixon Chemical Species Separation with an Iterative Least-Squares Estimation Method. *Magnetic Resonance in Medicine* 2004;51:35–45 doi: 10.1002/mrm.10675.
6. Hernando D, Haldar JP, Sutton BP, Ma J, Kellman P, Liang ZP. Joint estimation of water/fat images and field inhomogeneity map. *Magnetic Resonance in Medicine* 2008;59:571–580 doi: 10.1002/mrm.21522.
7. Yu H, Reeder SB, Shimakawa A, Brittain JH, Pelc NJ. Field map estimation with a region growing scheme for iterative 3-point water-fat decomposition. *Magnetic Resonance in Medicine* 2005;54:1032–1039 doi: 10.1002/mrm.20654.
8. Hernando D, Kellman P, Haldar JP, Liang ZP. Robust water/fat separation in the presence of large field inhomogeneities using a graph cut algorithm. *Magnetic Resonance in Medicine* 2010;63:79–90 doi: 10.1002/mrm.22177.
9. Lu W, Hargreaves BA. Multiresolution field map estimation using golden section search for water-fat separation. *Magnetic Resonance in Medicine* 2008;60:236–244 doi: 10.1002/mrm.21544.
10. Berglund J, Skorpil M. Multi-scale graph-cut algorithm for efficient water-fat separation. *Magnetic Resonance in Medicine* 2017;78:941–949 doi: 10.1002/mrm.26479.
11. Bydder M, Yokoo T, Hamilton G, et al. Relaxation effects in the quantification of fat using gradient echo imaging. *Magnetic Resonance Imaging* 2008;26:347–359 doi: 10.1016/j.mri.2007.08.012.

12. Yu H, Shimakawa A, Hines CDG, et al. Combination of complex-based and magnitude-based multiecho water-fat separation for accurate quantification of fat-fraction. *Magnetic Resonance in Medicine* 2011;66:199–206 doi: 10.1002/mrm.22840.
13. Yu H, Reeder SB, Shimakawa A, McKenzie CA, Brittain JH. Robust multipoint water-fat separation using fat likelihood analysis. *Magnetic Resonance in Medicine* 2012;67:1065–1076 doi: 10.1002/mrm.23087.
14. Glover GH, Schneider E. Three-point dixon technique for true water/fat decomposition with B0 inhomogeneity correction. *Magnetic Resonance in Medicine* 1991;18:371–383 doi: 10.1002/mrm.1910180211.
15. Triay Bagur A, Hutton C, Irving B, Gyngell ML, Robson MD, Brady M. Magnitude-intrinsic water–fat ambiguity can be resolved with multipeak fat modeling and a multipoint search method. *Magnetic Resonance in Medicine* 2019;82:460–475 doi: 10.1002/mrm.27728.
16. Bray TJ, Bainbridge A, Hall-Craggs MA, Zhang H. MAGORINO: Magnitude-only fat fraction and R2\* estimation with Rician noise modelling. 2021.
17. Sharma SD, Hernando D, Horng DE, Reeder SB. Quantitative susceptibility mapping in the abdomen as an imaging biomarker of hepatic iron overload. *Magnetic Resonance in Medicine* 2015;74:673–683 doi: 10.1002/mrm.25448.
18. Hamilton G, Yokoo T, Bydder M, et al. In vivo characterization of the liver fat 1H MR spectrum. *NMR in Biomedicine* 2011;24:784–790 doi: 10.1002/nbm.1622.
19. Bydder M, Kouzehkonan VG, Gao Y, Robson MD, Yang Y, Hu P. Constraints in estimating the proton density fat fraction. *Magnetic Resonance Imaging* 2020;66:1–8 doi: 10.1016/j.mri.2019.11.009.
20. Bydder M, Yokoo T, Yu H, Carl M, Reeder SB, Sirlin CB. Constraining the initial phase in water-fat separation. *Magnetic Resonance Imaging* 2011;29:216–221 doi: 10.1016/j.mri.2010.08.011.
21. Hernando D, Kramer JH, Reeder SB. Multipeak fat-corrected complex R2\* relaxometry: Theory, optimization, and clinical validation. *Magnetic Resonance in Medicine* 2013;70:1319–1331 doi: 10.1002/mrm.24593.
22. Roberts NT, Hernando D, Panagiotopoulos N, Reeder SB. Addressing concomitant gradient phase errors in time-interleaved chemical shift-encoded MRI fat fraction and R 2 \* mapping with a pass-specific phase fitting method. *Magnetic Resonance in Medicine* 2022:1–13 doi: 10.1002/mrm.29175.

23. Liu CY, McKenzie CA, Yu H, Brittain JH, Reeder SB. Fat quantification with IDEAL gradient echo imaging: Correction of bias from T1 and noise. *Magnetic Resonance in Medicine* 2007;58:354–364 doi: 10.1002/mrm.21301.
24. Peterson P, Månsson S. Fat quantification using multiecho sequences with bipolar gradients: Investigation of accuracy and noise performance. *Magnetic Resonance in Medicine* 2014;71:219–229 doi: 10.1002/mrm.24657.
25. Yu H, Shimakawa A, McKenzie CA, Brodsky E, Brittain JH, Reeder SB. Multiecho water-fat separation and simultaneous R<sup>2</sup> estimation with multifrequency fat spectrum modeling. *Magnetic Resonance in Medicine* 2008;60:1122–1134 doi: 10.1002/mrm.21737.
26. Hutton C, Gyngell ML, Milanese M, Bagur A, Brady M. Validation of a standardized MRI method for liver fat and T2 quantification. *PLoS ONE* 2018;13:1–12 doi: 10.1371/journal.pone.0204175.
27. Yu H, McKenzie CA, Shimakawa A, et al. Multiecho reconstruction for simultaneous water-fat decomposition and T2\* estimation. *Journal of Magnetic Resonance Imaging* 2007;26:1153–1161 doi: 10.1002/jmri.21090.
28. Irving B, Hutton C, Dennis A, et al. Deep quantitative liver segmentation and vessel exclusion to assist in liver assessment. *Communications in Computer and Information Science* 2017;723:663–673 doi: 10.1007/978-3-319-60964-5\_58.
29. Altman DG, Bland JM. *Measurement in Medicine: The Analysis of Method Comparison Studies*. The Statistician 1983;32:307 doi: 10.2307/2987937.
30. Peterson P, Månsson S. Fat quantification using multiecho sequences with bipolar gradients: Investigation of accuracy and noise performance. *Magnetic Resonance in Medicine* 2014;71:219–229 doi: 10.1002/mrm.24657.
31. Peng H, Zou C, Cheng C, et al. Fat-water separation based on Transition REgion Extraction (TREE). *Magnetic Resonance in Medicine* 2019;82:436–448 doi: 10.1002/mrm.27710.